Insights into cathodic hydrogen charging - surface morphology evolution

Downloaded from: https://research.chalmers.se, 2026-04-14 22:46 UTC

Citation for the original published paper (version of record):
Qin, X., Shi, Y., Malladi, B. et al (2026). Insights into cathodic hydrogen charging - surface morphology evolution. International Journal of Hydrogen Energy, 220.
http://dx.doi.org/10.1016/j.ijhydene.2026.154155

N.B. When citing this work, cite the original published paper.

research.chalmers.se offers the possibility of retrieving research publications produced at Chalmers University of Technology. It covers all kind of research output: articles, dissertations, conference papers, reports etc. since 2004. research.chalmers.se is administrated and maintained by Chalmers Library

(article starts on next page)

International Journal of Hydrogen Energy 220 (2026) 154155

Contents lists available at ScienceDirect

International Journal of Hydrogen Energy

journal homepage: www.elsevier.com/locate/he

Insights into cathodic hydrogen charging - surface morphology evolution

Xiao Qin [a,b], Yao Shi [a], Sri Bala Aditya Malladi [a], Huiqun Liu [b], Lars Nyborg [a], Yu Cao [a,*]

[a] Department of Industrial and Materials Science, Chalmers University of Technology, Gothenburg, 41296, Sweden
[b] School of Materials Science and Engineering, Central South University, Changsha, 410083, PR China

ARTICLE INFO

Keywords:
Surface morphology
Cathodic hydrogen charging
Hydrogen uptake
Hydrogen embrittlement

ABSTRACT

Cathodic hydrogen charging is widely used to introduce hydrogen into metals for studying hydrogen embrittlement (HE). However, its side effect on surface morphology and surface chemistry have received relatively little attention. In this study, 316L austenitic stainless steel is charged in three electrolytes: H_2SO_4, NaCl and NaOH solutions. The induced changes in surface morphology depend on the charging conditions and the initial surface roughness. In H_2SO_4, surface cracking occurs and the hydrogen content increases sharply with increasing current density. Surface roughening significantly suppresses hydrogen-induced cracking, likely due to enhanced hydrogen recombination on rougher surfaces. In contrast, charging in NaOH and NaCl does not produce surface cracking because of the relatively low hydrogen uptake. However, surface deposits originating from trace impurities in the electrolyte are observed. Among the three electrolytes, NaCl produces the least change in surface morphology. Surface cracking and deposition may influence HE behavior and should not be overlooked.

1. Introduction

Cathodic hydrogen charging is one of the most effective approaches to introduce hydrogen into metals and study their susceptibility to hydrogen embrittlement (HE) [1–4]. Compared with thermal gaseous hydrogen charging, this method has the advantages of low cost, simple operation, and high safety. In this method, hydrogen is generated by the hydrogen evolution reaction (HER) [5,6] in aqueous electrolytes and subsequently adsorbs and diffuses into the metallic substrate. However, the hydrogen evolution process is inevitably accompanied by electrochemical interactions between the electrolyte, current, hydrogen and substrate, which can alter the surface morphology through localized corrosion and mechanical damage [7–10]. Most studies on HE has focused primarily on the material response after hydrogen has been absorbed into the metals [11,12], while limited data exist on the initial adsorption/absorption processes of hydrogen at the metal surface. Understanding how surface morphology evolves during cathodic charging is thus crucial for bridging the knowledge gap between electrochemical hydrogen generation and hydrogen-assisted mechanical degradation. Recent studies have demonstrated that electrolyte composition, surface roughness and current density for cathodic hydrogen charging are important factors that significantly affect HE [1,13–15] behavior.

The surface state of material is strongly influenced by industrial manufacturing practices, such as machining and forming, which often introduce roughness, residual stress, and plastic deformation. Many studies have sought to elucidate the effects of machining-induced microstructural changes on electrochemical processes, with a primary focus on the corrosion and catalytic performance [16–20]. It has been reported that increased surface roughness, residual stress and dislocation density generally promote the corrosion susceptibility of metals such as copper [16], pipeline steel [17] and Ti–6Al–4V [18]. For a rough surface, electrons near asperity peaks can escape more easily than those in valleys, leading to local fluctuation in the electron work function and thereby accelerating surface corrosion [19]. Moreover, surface roughness has been shown to modify HER kinetics. It is reported that rough mild steel electrodes exhibit lower Tafel slopes compared to smooth electrodes, indicating that roughening can reduce the kinetic barrier of HER [20].

Apart from the surface state, the type of electrolyte plays a critical role in determining hydrogen charging behavior. Commonly employed electrolytes for cathodic charging include H_2SO_4, NaCl, and NaOH solutions, which provide different proton concentrations and thereby influence HER rates [21]. Likewise, the applied current density governs the hydrogen generation rate at the surface, which in turn controls hydrogen uptake and the extent of surface morphological changes. Despite the recognized importance, systematic studies addressing the combined influence of electrolyte composition, current density, and surface roughness on surface morphological evolution during hydrogen

* Corresponding author.
E-mail address: yu.cao@chalmers.se (Y. Cao).

https://doi.org/10.1016/j.ijhydene.2026.154155
Received 24 December 2025; Received in revised form 17 February 2026; Accepted 19 February 2026
Available online 21 February 2026
0360-3199/© 2026 The Authors. Published by Elsevier Ltd on behalf of Hydrogen Energy Publications LLC. This is an open access article under the CC BY license (http://creativecommons.org/licenses/by/4.0/).

charging remain limited. This knowledge gap is particularly relevant for structural alloys in hydrogen energy applications.

Austenitic stainless steels (ASS), especially 316L, are widely employed in hydrogen-containing environments such as pressure vessels, valves, and fuel cell components, owing to their low hydrogen diffusivity and excellent corrosion resistance compared with ferritic and martensitic steels [22–25]. Nevertheless, even in these alloys, surface-mediated hydrogen processes can substantially affect long-term reliability by reducing ductility and promoting premature brittle failure. In this work, we systematically investigate the effects of cathodic hydrogen charging parameters, including electrolyte composition and current density, on the surface morphology evolution of 316L. The influence of surface roughness, which may alter hydrogen absorption behavior, was also examined. By establishing correlations between charging conditions and surface states, this study provides new insights into the early-stage interactions between hydrogen and metal surfaces. The results aim to enhance understanding of hydrogen uptake mechanisms and to support the optimization of electrochemical charging protocols for both fundamental research and engineering applications.

2. Experimental procedures

2.1. Material

The experimental material used in this work was commercial AISI 316L austenitic stainless steel with a chemical composition of Fe-16.7Cr-10.1Ni-2.04Mo-1.6Mn-0.02C-0.39Si-0.58Cu (wt%). The as-received cold-drawn bars were solution-annealed at 1050 °C for 1 h. The microstructure after the solution annealing in Fig. 1 shows equiaxed grains with an average grain size of ~40 μm. The inverse pole figure (IPF) map in Fig. 1a reveals a random grain orientation, indicating that the impact of crystallographic texture can be considered negligible. The SEM image in Fig. 1b shows a small number of inclusions, primarily composed of copper and manganese sulfides.

2.2. Hydrogen charging, hydrogen content and hydrogen entry

The sample used was a disc with a diameter of 10 mm and a thickness of 2 mm. To obtain different surface roughness levels, the samples were ground or polished sequentially using 500# SiC sandpaper (grit size 30 μm) and diamond suspensions of 9 μm, 3 μm and 1 μm, respectively. To study the effect of electrolyte composition and current density on hydrogen charging, the samples were ground and polished with a 1 μm diamond suspension. Prior to electrochemical hydrogen charging, all samples were ultrasonically cleaned in ethanol for 10 min and dried with compressed air. Hydrogen charging was conducted in a two-electrode setup, with the specimen serving as the cathode (working electrode) and the platinum wire as the anode (counter electrode). A potentiostat (Solartron 1287) was employed to apply constant current densities of 0.3, 3, and 30 mA/cm^2 under galvanostatic mode. Three aqueous solutions: 0.2 M H_2SO_4, 3 wt% NaCl and 0.2 M NaOH were used as the electrolyte. To enhance hydrogen absorption, 1 g/L $Na_2HAsO_4{\cdot}7H_2O$ was added as a recombination poison to suppress hydrogen evolution. All chemical reagents used in the experiment were analytical grade: H_2SO_4 (98%, from VWR), NaCl (≥98%, from VWR), NaOH (≥97%, from Sigma-Aldrich) and $Na_2HAsO_4{\cdot}7H_2O$ (≥98%, from Sigma-Aldrich). The temperature and duration for charging were maintained at 80 ± 5 °C for 10 h. The total hydrogen content was measured using the Bruker G8 GALILEO ONH elemental analyzer based on the inert gas fusion method.

Hydrogen bubbles generated during charging were captured using an electrochemical cell combined with an optical microscope (OM, Zeiss Axioscope 7). The experimental setup is given schematically in Fig. 2. The specimen was a circular disc with a diameter of 12 mm and a thickness of 2 mm, and the exposed area of the specimen was within the O-ring region with a diameter of 8 mm. A Pt wire was used as the counter electrode and was placed on top of the cell. OM images of the specimen exposed were taken through the electrolyte during hydrogen-charging with a current density of 0.5 mA/cm^2, revealing hydrogen bubbles trapped on the specimen surface.

2.3. Surface morphology and chemical characterization

The surface morphologies of the samples after hydrogen charging were examined by optical microscopy (Zeiss Axioscope 7) and scanning electron microscopy (LEO Gemini 1550 SEM). The chemistry of the

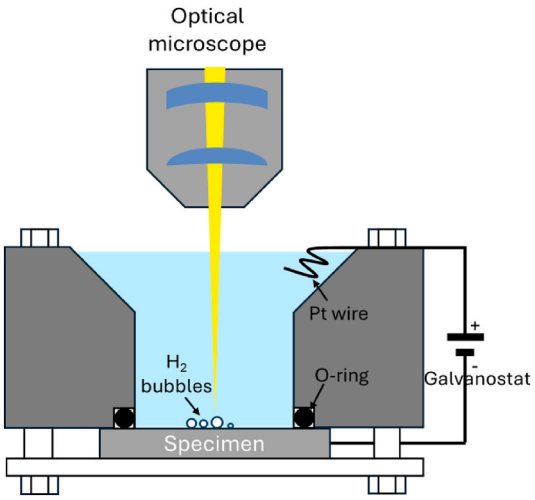

Fig. 2. Schematic diagram of the electrochemical cell combined with OM used for in-situ observation of H_2 bubbles.

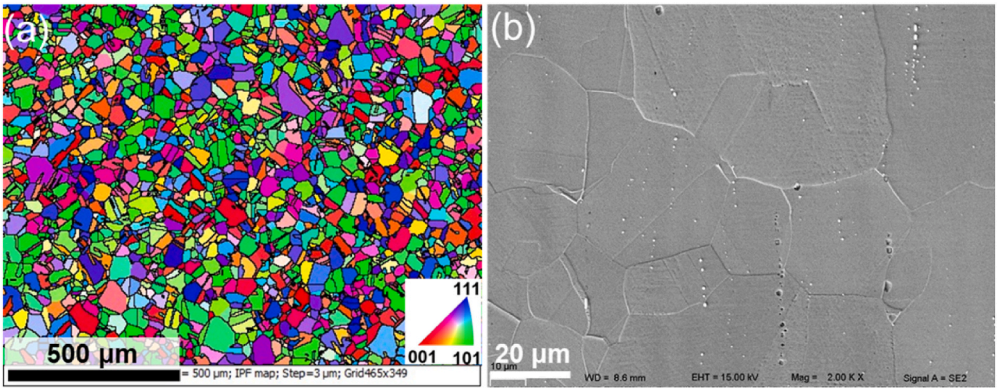

Fig. 1. Microstructure of solution annealed 316L: (a) IPF map and (b) SE image.

surface was analysed by means of a PHI VersaProbe III Scanning XPS microprobe (ULVAC-PHI) equipped with a monochromatic Al Kα X-ray source (hγ = 1486.6 eV). The X-ray beam size was 100 μm and take-off angle was 45°. The acquired spectra were evaluated using Multipak software.

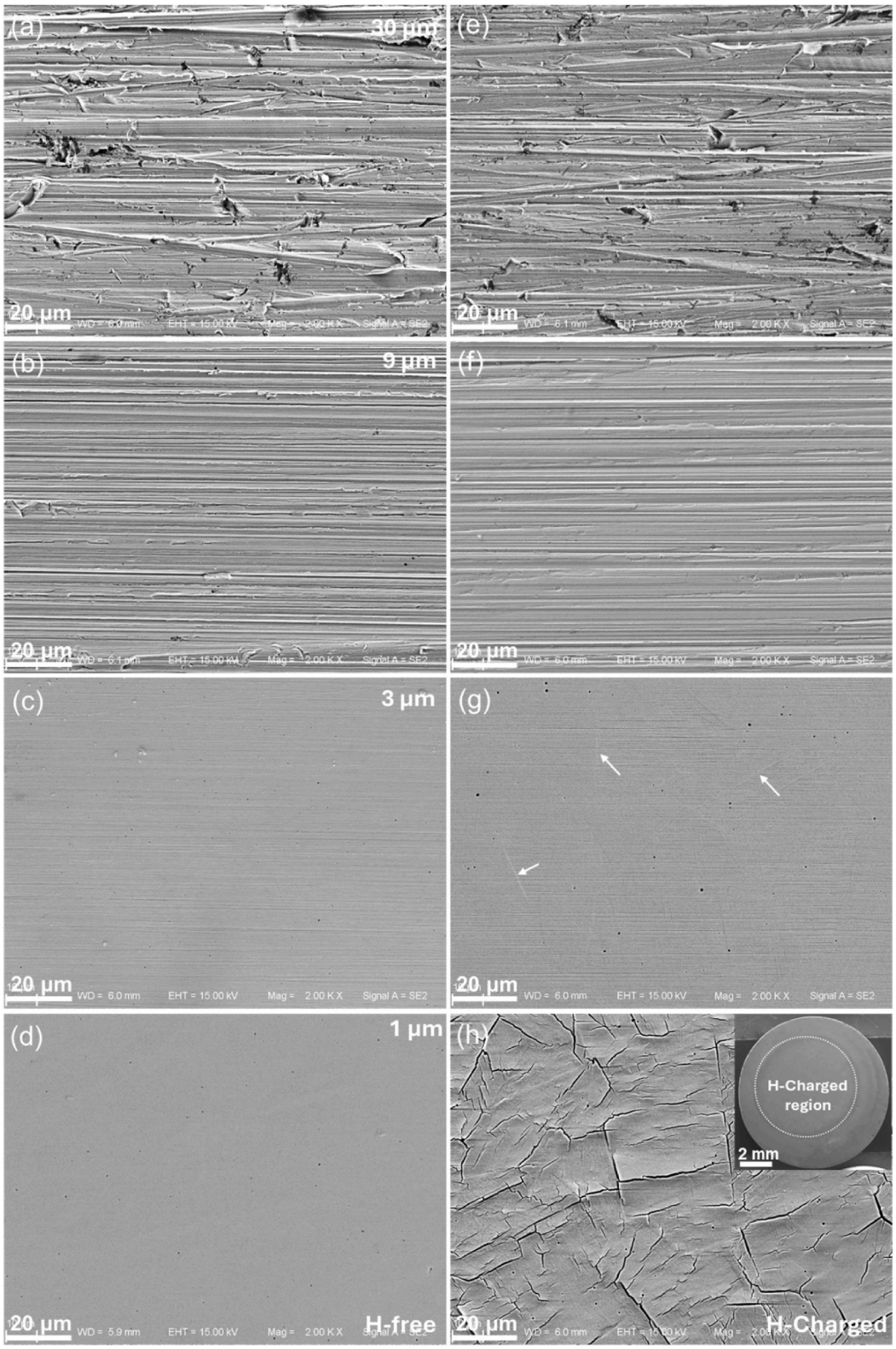

Fig. 3. Surface morphologies of H-free (a-d) and H-charged (e-h) 316L. The samples were initially ground to obtain different surface roughness levels using grit size of (a)(e) 30 μm, (b)(f) 9 μm, (c)(g) 3 μm, (d)(h) 1 μm. The H charging was conducted at a current density of 30 mA/cm^2 in 0.2 M H_2SO_4 for 10h.

3. Results

3.1. Hydrogen charging induced cracking in acidic electrolyte

3.1.1. Effect of roughness

Fig. 3a–d shows the surface morphologies of samples after grinding and polishing with different grit sizes. As depicted in Fig. 3a, the surface ground with 30 μm grit exhibited deep grooves and surface tearing, indicative of surface deformation and mechanical wear. With the decrease in grit size, the grooves became progressively shallower and narrower (Fig. 3b and c), indicating a gradual reduction in deformation depth and mechanical damage. The surface polished with 1 μm grit appeared smooth and nearly free of scratches (Fig. 3d). Fig. 3e–h shows surface morphologies of hydrogen-charged samples prepared with different grit sizes. Hydrogen charging did not noticeably alter the surface morphology for samples ground with grits larger than 3 μm (Fig. 3e and f). In the H-charged sample ground with 3 μm grit, occasional protrusions along grain boundaries were observed, as marked by white arrows (Fig. 3g). In contrast, hydrogen charged sample polished with 1 μm grit exhibited severe surface cracking (Fig. 3h). The observed surface deformation and protrusions near the crack suggested the presence of large strain induced by hydrogen uptake. Overall, surface roughness influences the hydrogen induced cracking behavior of 316L when charged in 0.2 M H_2SO_4.

To clarify the relationship between surface cracking and hydrogen uptake, the hydrogen content of samples with different surface roughness after hydrogen charging was measured, as summarized in Table 1. When the grit size was ≥9 μm, the hydrogen content remained around 6 ppm. In contrast, the sample polished with 1 μm grit exhibited a significantly higher hydrogen content of 17.50 ppm. The pronounced surface cracking observed in the sample polished with 1 μm grit corresponds to this elevated hydrogen content, whereas the intact surface of the sample polished with 9 μm grit had a lower hydrogen content. These results indicate that surface cracking accelerated hydrogen uptake by increasing effective surface area and facilitating hydrogen absorption.

To elucidate the effect of surface roughness on hydrogen absorption, in-situ cathodic hydrogen charging combined with optical observation were performed. A low charging current density of 0.5 mA/cm^2 was used, as higher current densities would accelerate the hydrogen evolution reaction and generate excessive hydrogen bubbles, thereby obscuring optical observation. Optical micrographs in Fig. 4 illustrate the evolution of hydrogen bubbles over charging time for samples previously ground with 9 μm and 1 μm grits, respectively. The entire hydrogen charging duration was 10 min. However, as the bubble evolution remained consistent at later times, only the results from the first 3 min are presented. The grooves on the rough surface were clearly visible (Fig. 4a–a_3) while the smooth surface appeared nearly scratch-free (Fig. 4b–b_3). With increasing charging time, hydrogen bubbles indicated by white arrows formed and grew on the surface, with the number increasing over time. The density of hydrogen bubbles on the rough surface was notably higher than that on the smooth one, indicating that a greater fraction of hydrogen escaped as molecular hydrogen. Conversely, the smooth surface showed fewer and smaller hydrogen bubbles on average, implying more absorbed hydrogen. In summary, surface roughening reduces hydrogen absorption by promoting hydrogen recombination and thereby reducing hydrogen content, while smooth surfaces favor hydrogen uptake, leading to higher hydrogen content and surface cracking.

Table 1
Total hydrogen content of samples ground to different grits after being charged in 0.2 M H_2SO_4 at a current density of 30 mA/cm^2 for 10h.

Grid size	30 μm	9 μm	1 μm
Total H content	6.20 ppm	5.78 ppm	17.50 ppm

3.1.2. Effect of current density

Fig. 5a shows the evolution of cell potential (E) during hydrogen charging at different current densities in 0.2 M H_2SO_4 aqueous solution. As the applied current density i increased from 0.3 mA/cm^2 to 30 mA/cm^2, the cell potential decreased significantly, from approximately −2.0 V to about −3.0 V. At constant current, the potential oscillated with time, which become more pronounced at higher charging currents. These fluctuations are attributed to the dynamic formation, growth, and detachment of hydrogen bubbles on the surface during the hydrogen evolution reaction, which alters the effective electrode area and local resistance.

The surface morphologies after hydrogen charging at different current densities in 0.2 M H_2SO_4 aqueous solution are shown in Fig. 5b–d. At a current density of 0.3 mA/cm^2, slip bands were observed (insert in Fig. 5b), indicating plastic deformation caused by hydrogen-induced stress. As the current density increased, cracking was observed (Fig. 5c and d). Localized corrosion was also present, as marked by the white arrows in the insert of Fig. 5c. In Fig. 5d, most cracks appear to initiate from slip bands, as implied by their straight morphology, as well as from grain boundaries. The crack densities, defined as crack length per unit area (ρ_l) or crack number per unit area (ρ_{nr}), are summarized in Table 2. There were no cracks detected at 0.3 mA/cm^2. When the current density increased from 3 mA/cm^2 to 30 mA/cm^2, both crack-density metrics nearly doubled. This correlation is supported by the total hydrogen content measured after hydrogen charging at different current densities (Table 3). As the current density increased from 0.3 mA/cm^2 to 30 mA/cm^2, the hydrogen content increased from 2.08 ppm to 17.50 ppm, an increase of 8.4 times. The sample charged at 30 mA/cm^2 exhibited extensive surface cracking, while the sample charged at 0.3 mA/cm^2 displayed only a few slip bands. Higher current densities led to greater hydrogen uptake, resulting in higher internal stress and more severe cracking. These observations confirm that increasing current density promotes surface cracking, which in turn facilitates further hydrogen uptake.

3.2. Hydrogen charging induced deposition in neutral and alkaline electrolyte

Fig. 6a shows the cell potential versus time during hydrogen charging in 3 wt% NaCl solution. Similar to the behavior observed in H_2SO_4 solution, the potential decreased with increasing current density. At the highest current density of 30 mA/cm^2, potential fluctuations were likely to be caused by hydrogen bubbles formed on the surface due to recombination of atomic hydrogen. Notably, at identical current densities, the cell potential in NaCl solution was lower than that in H_2SO_4. For instance, at 30 mA/cm^2, the potential reached −3.7 V in NaCl solution, which was lower than that in H_2SO_4 solution (−3.0 V). Fig. 6b–d shows the corresponding surface morphologies after charging in NaCl solution at different current densities. At 0.3 and 3 mA/cm^2, no significant surface changes were observed (Fig. 6b and c). At the highest current density of 30 mA/cm^2, nanoparticle-like surface deposits were detected, as revealed in the insert of Fig. 6d. In contrast to the H_2SO_4 condition, hydrogen charging in NaCl did not induce surface cracking at any current density. It was also worth noting that, compared with the H-free sample (Fig. 3d), hydrogen charging caused certain inclusions to detach, leaving pits, as shown in Fig. 6d. Hydrogen accumulation at inclusions during cathodic hydrogen charging has been reported in previous studies [26,27].

The surface chemistry of 316L after hydrogen charging in 3 wt% NaCl solution was investigated using XPS, as shown in Fig. 7. The as-received sample exhibited primary peaks of Fe, Cr, Ni, Mn, consistent with the steel composition, along with signals from O and C originating from the native surface oxide and adventitious carbon. With hydrogen charging, additional elements such as Mg, Cu, and Pb were found on the surface. Since deionized water was used as the solvent when preparing electrolyte, these elements might come from the impurity in the

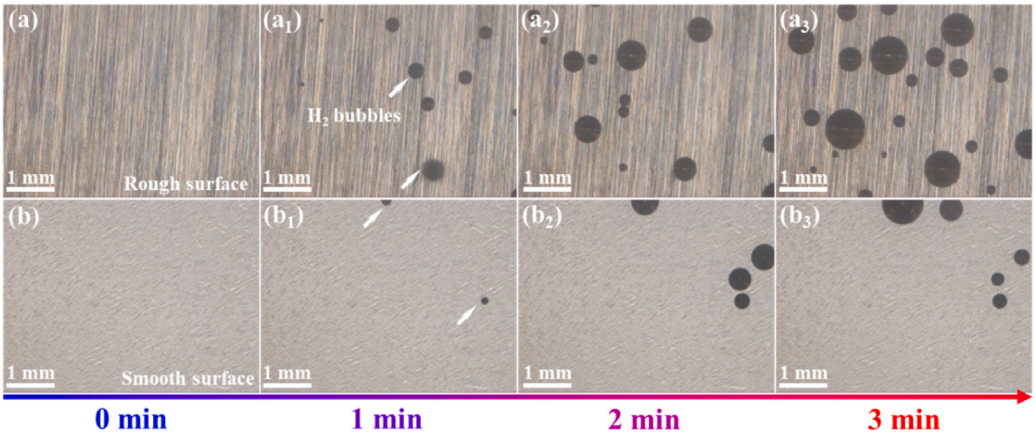

Fig. 4. In situ optical microscopy (OM) observations of hydrogen bubble evolution during cathodic hydrogen charging for samples with different roughness levels obtained using grit size of 9 μm (a-a_3) and 1 μm (b-b_3). Hydrogen charging was performed at current density of 0.5 mA/cm^2 in 0.2 M H_2SO_4 at 25 °C.

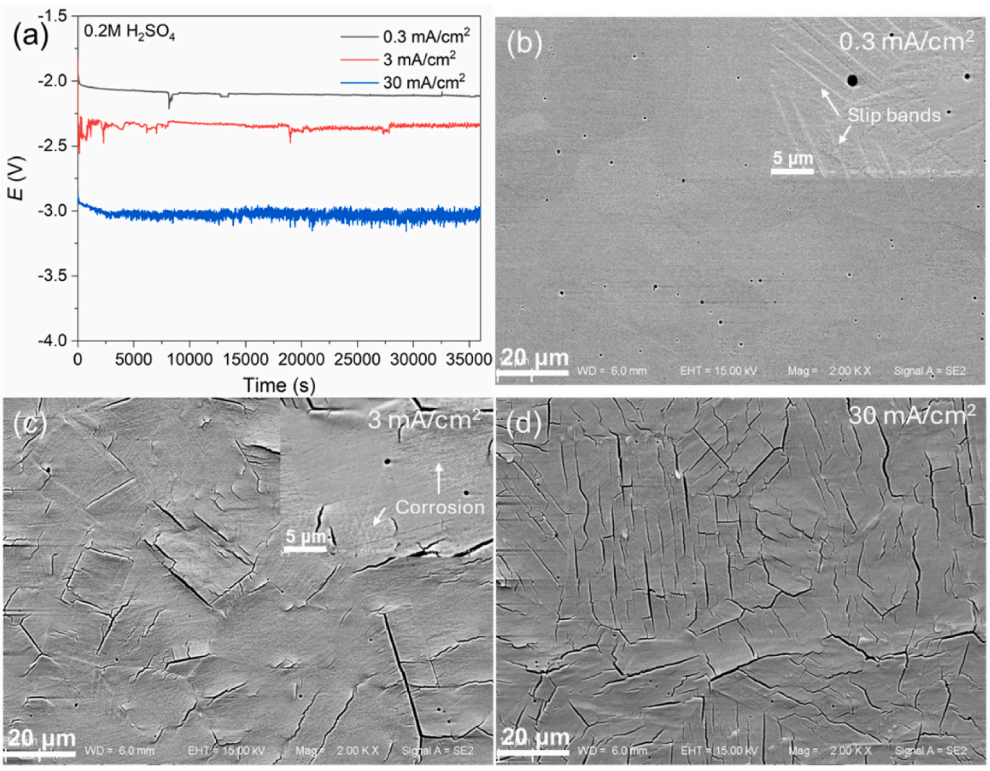

Fig. 5. (a) Potential versus hydrogen charging time in 0.2 M H_2SO_4 electrolyte. Surface morphologies after hydrogen charging at different current densities of (b) 0.3 mA/cm^2, (c) 3 mA/cm^2, and (d) 30 mA/cm^2.

Table 2
Crack density in 316L caused by hydrogen charging.

Current density (mA/cm^2)	0.3	3	30
ρ_l (10^4 μm mm^{-2})[a]	-	1.1	1.9
ρ_{nr} (10^5 mm^{-2})[b]	-	2.7	5.3

[a] : ρ_l is defined as the length of cracks per unit area.
[b] : ρ_{nr} is defined as the number of cracks per unit area.

chemicals. The deposits observed in Fig. 6d were presumed to be related to these impurities, with Mg showing the strongest association, as the intensity of Mg increased significantly with the current density. Interestingly, according to the product specifications, the maximum combined content of Mg and alkali metals in the NaCl was only 100 ppm.

Table 3
Total hydrogen content of samples charged under different current densities in 0.2 M H_2SO_4 for 10h. All samples were polished using a 1 μm diamond suspension.

Current density	0.3 mA/cm^2	3 mA/cm^2	30 mA/cm^2
Total H content	2.08 ppm	10.50 ppm	17.50 ppm

XPS region spectra of C 1s, O 1s, Fe 2p, Cr 2p and Mg 2p, as well as Mg KLL obtained from the as-received sample and the specimen charged at a current density of 30 mA/cm^2 are shown in Fig. 8. The C 1s peak from adventitious carbon located at a binding energy (BE) of 284.8 eV was used as the reference. For the as received 316L, the surface was dominated by iron and chromium oxides/hydroxides, with small

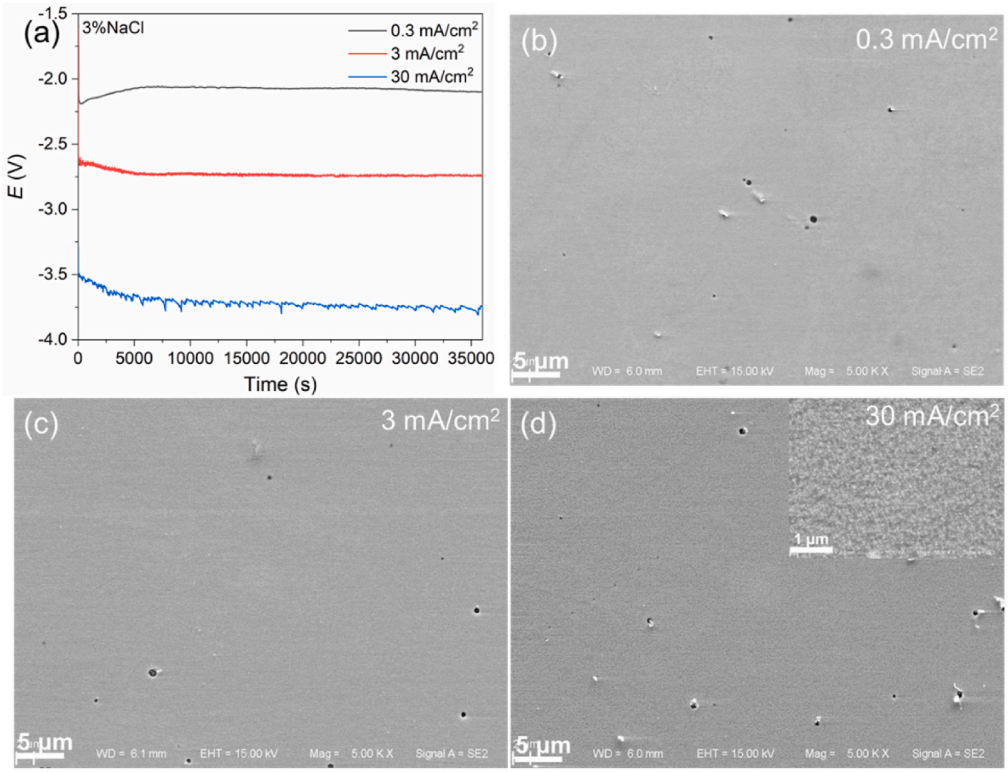

Fig. 6. (a) Potential versus hydrogen charging time in 3 wt% NaCl solution. Surface morphologies after hydrogen charging at different current densities of (b) 0.3 mA/cm^2, (c) 3 mA/cm^2, (d) 30 mA/cm^2.

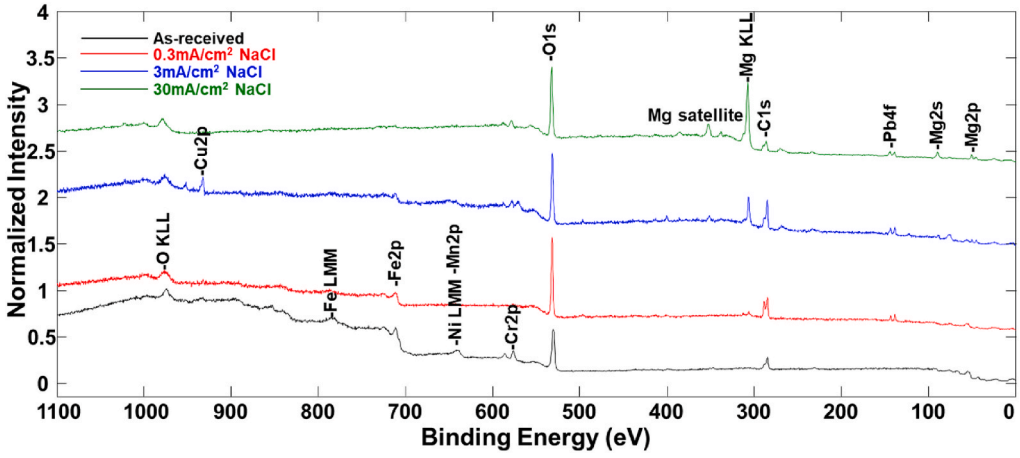

Fig. 7. XPS survey spectra of 316L after hydrogen-charging in 3 wt% NaCl solution.

amounts of metallic Fe and Cr also present. After hydrogen charging, these metallic components nearly disappeared. For the O 1s core level, the fraction of OH^- component increased significantly, consistent with the shift of Cr 2p towards higher BE after charging, as revealed in Fig. 8. The Mg 2p was located at 49.7 eV (referenced to adventitious C1s at 284.8 eV). Identification of its chemical state was challenging. The reported Mg 2p BEs vary widely in the literature for the same chemical state. Skaanvik et al. [28] attributed the discrepancies to charge referencing procedures and emphasized the advantage of methods independent of electrostatic charging. Therefore, Auger parameter α, defined as the sum of the binding energy of a core level electron E_b and the kinetic energy of an Auger electron E_k, was calculated. Using Mg 2p and Mg KLL, a α value of 1230.4 eV was obtained, consistent with $Mg(OH)_2$ [28]. Tian et al. [29] reported that in simulated artificial seawater, an increase in cathode potential led to the deposition of $Mg(OH)_2$ and $MgCO_3$. However, the absence of a component located at ~290.2 eV suggested that the formation of $MgCO_3$ [28] was less likely. When charging in 3 wt% NaCl solution, $Mg(OH)_2$ deposits detected in this study were attributed to the impurities in the reagents.

Fig. 9a shows the cell potential as a function of charging time at different current densities in 0.2 M NaOH solution. As the current density increased, the potential gradually decreased. At both low and high current densities, the potential exhibited oscillations during charging. Fig. 9b presents the surface morphology after charging at 0.3 mA/cm^2, where discrete particles were found on the surface. With increasing current density, a network-like layer developed (Fig. 9c), with characteristic dimension of a few hundred nm (see the insert in Fig. 9c). At 30 mA/cm^2, the surface became fully covered by ellipsoidal particles with

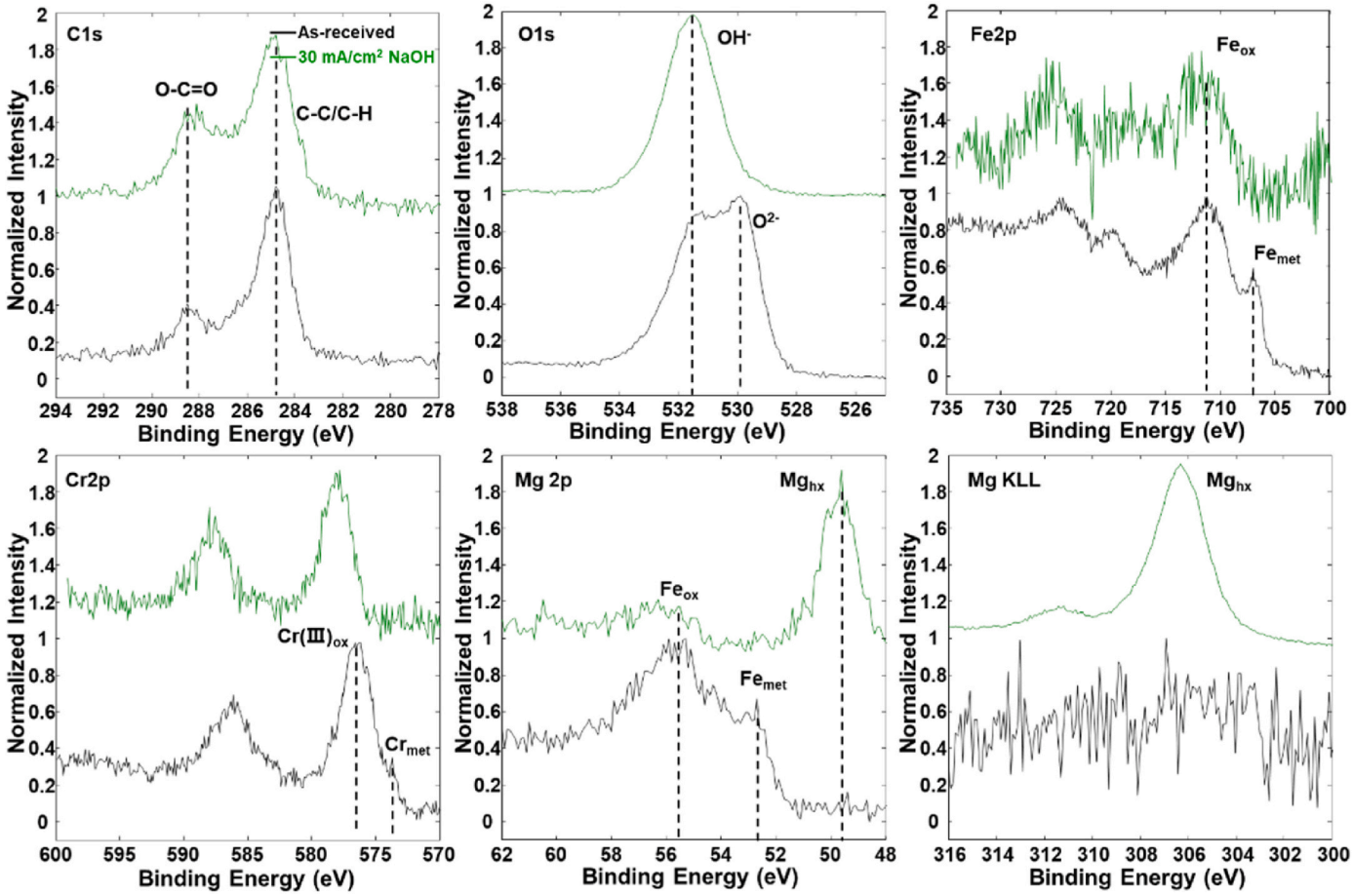

Fig. 8. XPS region spectra from the as-received sample and the specimen charged at a current density of 30 mA/cm^2 in 3 wt% NaCl solution.

an average size on the order of ~1 μm (inset of Fig. 9d).

XPS analysis was performed to further explore the surface chemistry associated with the observed morphologies. The survey spectra in Fig. 10 revealed pronounced Pb peaks in the hydrogen-charged samples, in contrast to the as-received 316L, which exhibited only the expected Fe, Cr, Ni, Mn, O and C signals. Combined with the surface morphology in Fig. 8, this indicates that hydrogen charging led to lead-rich deposition. The high-resolution XPS region spectra in Fig. 11 provides further insight into the chemical nature of these deposits. After hydrogen charging, a well-defined Pb 4f doublet appeared, with Pb $4f_{7/2}$ located at 138.2 eV. In the Fe 2p and Cr 2p regions, only background signals were detected, consistent with the steel substrate being covered by the surface deposits. The C 1s spectrum revealed a strong component at 288.7 eV referenced to adventitious C1s at 284.8 eV. For the O 1s core level, the component corresponding to Cr/Fe oxide (O^{2-}) disappeared and O 1s was located at 530.8 eV after hydrogen charging. These features suggest that the deposits correspond to a hydrated lead carbonate species, most likely hydrocerussite ($2PbCO_3{\cdot}Pb(OH)_2$). The binding energies observed for C 1s, O 1s and Pb $4f_{7/2}$ are consistent with the values reported for hydrocerussite in the literature [30]. Although the NaOH reagent contained only ~5 ppm Pb according to its specification, this trace impurity evidently led to significant deposition during hydrogen charging. These findings demonstrate that even trace electrolyte impurities can strongly influence the resulting surface morphology.

3.3. Hydrogen uptake in different electrolytes

As shown in Figs. 5, 6 and 9, cathodic hydrogen charging in the three different electrolytes resulted in different surface morphologies, which could in turn affect the hydrogen uptake in the steel. Table 4 summarizes the total hydrogen content of samples charged in each electrolyte at a current density of 30 mA/cm^2 for 10h. Despite the identical current density, the resulting hydrogen contents differ markedly. The highest hydrogen content was obtained in 0.2 M H_2SO_4, followed by 0.2 M NaOH, while the lowest was measured in 3 wt% NaCl. Hydrogen charging in 0.2 M H_2SO_4 induced surface cracking, which facilitated further hydrogen uptake. In contrast, samples charged in 3 wt% NaCl and 0.2 M NaOH maintained intact surfaces and exhibited lower hydrogen contents, indicating the presence of a critical hydrogen concentration required to initiate hydrogen-induced cracking. It is also noteworthy that the hydrogen content in 3 wt% NaCl is only about half of that in 0.2 M NaOH. To eliminate the influence of surface deposits, the H-charged sample in 0.2 M NaOH was gently polished with 1 μm grit for 1 min to remove the deposits. The hydrogen content was reduced from 3.3 to 2.0 ppm (Table 4) due to the removal of hydrated lead carbonate species deposited (likely hydrocerussite as confirmed by XPS), at least partly. Still, the hydrogen content was higher than that obtained in 3 wt % NaCl. This may be attributed to the available hydrogen source, as discussed in section 4.2.

4. Discussion

Cathodic hydrogen charging introduces hydrogen into the sample through the hydrogen evolution reaction (HER) at the cathode, which proceeds via the Volmer-Tafel-Heyrovsky mechanism, as given in equations (1)–(6). The specific reaction steps depend on the pH value of the electrolyte.

$H^+ + M + e^- \rightleftharpoons M\text{-}H_{ads}$ (1) (Volmer-acid)

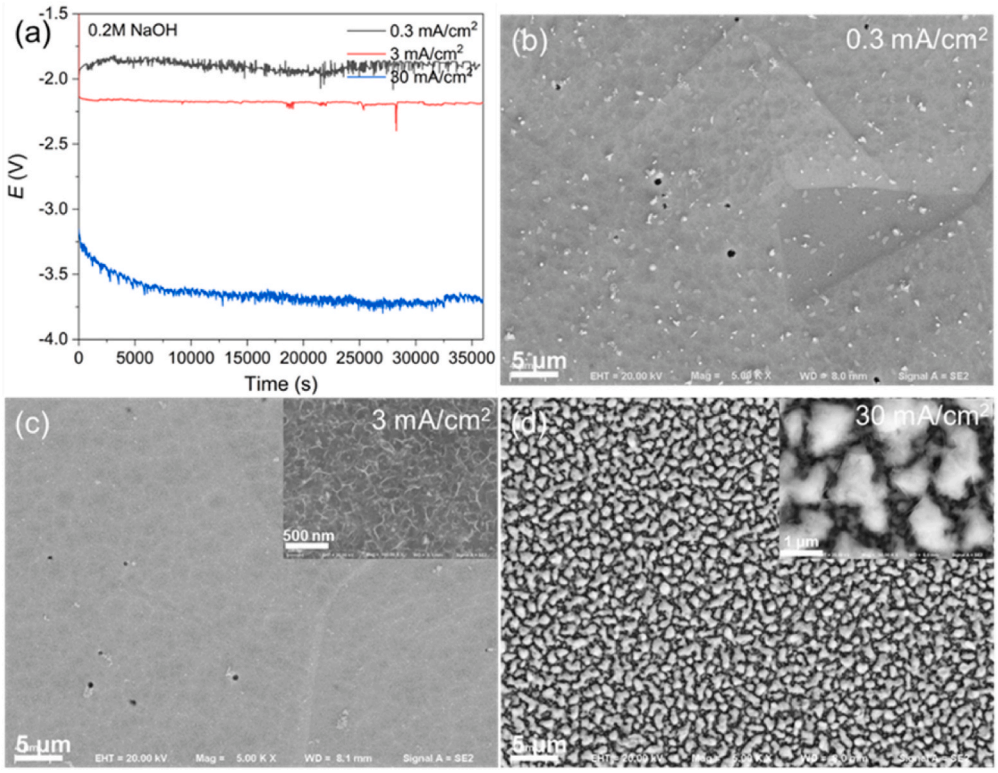

Fig. 9. (a) Potential versus hydrogen charging time in 0.2 M NaOH and surface morphologies corresponding to hydrogen charging at different current densities of (b) 0.3 mA/cm^2, (c) 3 mA/cm^2, and (d) 30 mA/cm^2.

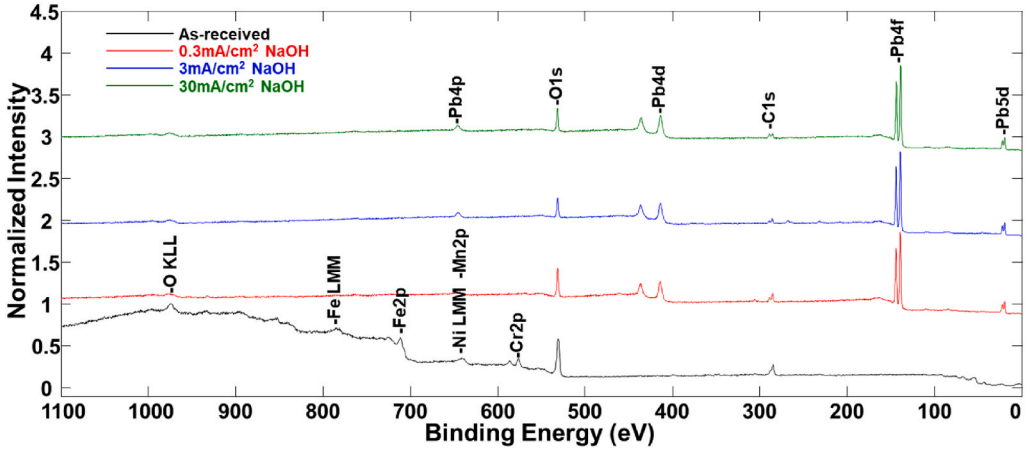

Fig. 10. XPS survey spectra of 316L after hydrogen charging in 0.2 M NaOH.

$H_2O + M + e^- \rightleftharpoons M\text{-}H_{ads} + OH^-$ (2) (Volmer-neutral/base)

$H_{ads} + H_{ads} \rightleftharpoons H_2$ (3) (Tafel)

$H^+ + H_{ads} + e^- \rightleftharpoons H_2$ (4) (Heyrovsky-acid)

$H_2O + H_{ads} + e^- \rightleftharpoons H_2 + OH^-$ (5) (Heyrovsky-neutral/base)

$M\text{-}H_{ads} \rightleftharpoons M\text{-}H_{abs}$ (6) (adsorption H to absorption H)

In the Volmer step, hydrogen ions are reduced (Eqs. (1) and (2)) and adsorb onto the metal surface (M–H_{ads}), providing the precursor for hydrogen absorption into the metal lattice (Eq. (6)). Alternatively, adsorbed hydrogen can also recombine to form molecular hydrogen via the Tafel and/or Heyrovsky steps (Eqs. (3)–(5)). The resulting H_2 gas escapes as bubbles, reducing the amount of hydrogen available for absorption. In this work, the surface morphology changes caused by cathodic charging are related to surface roughness, current density and electrolyte chemistry. The following discussion focuses on the roles of these factors.

4.1. Roughening inhibits hydrogen absorption and surface cracking

Table 1 shows that the hydrogen content of the rough surface is significantly lower than that of the smooth sample under the same hydrogen charging conditions. This means that roughening effectively reduces hydrogen uptake. Fig. 3 shows that at the same current density, roughened samples exhibited a greater number and larger volume of hydrogen bubbles compared with polished ones, implying that the rough surface provides more active sites for catalytic hydrogen recombination. A schematic of hydrogen uptake on rough and smooth surfaces during

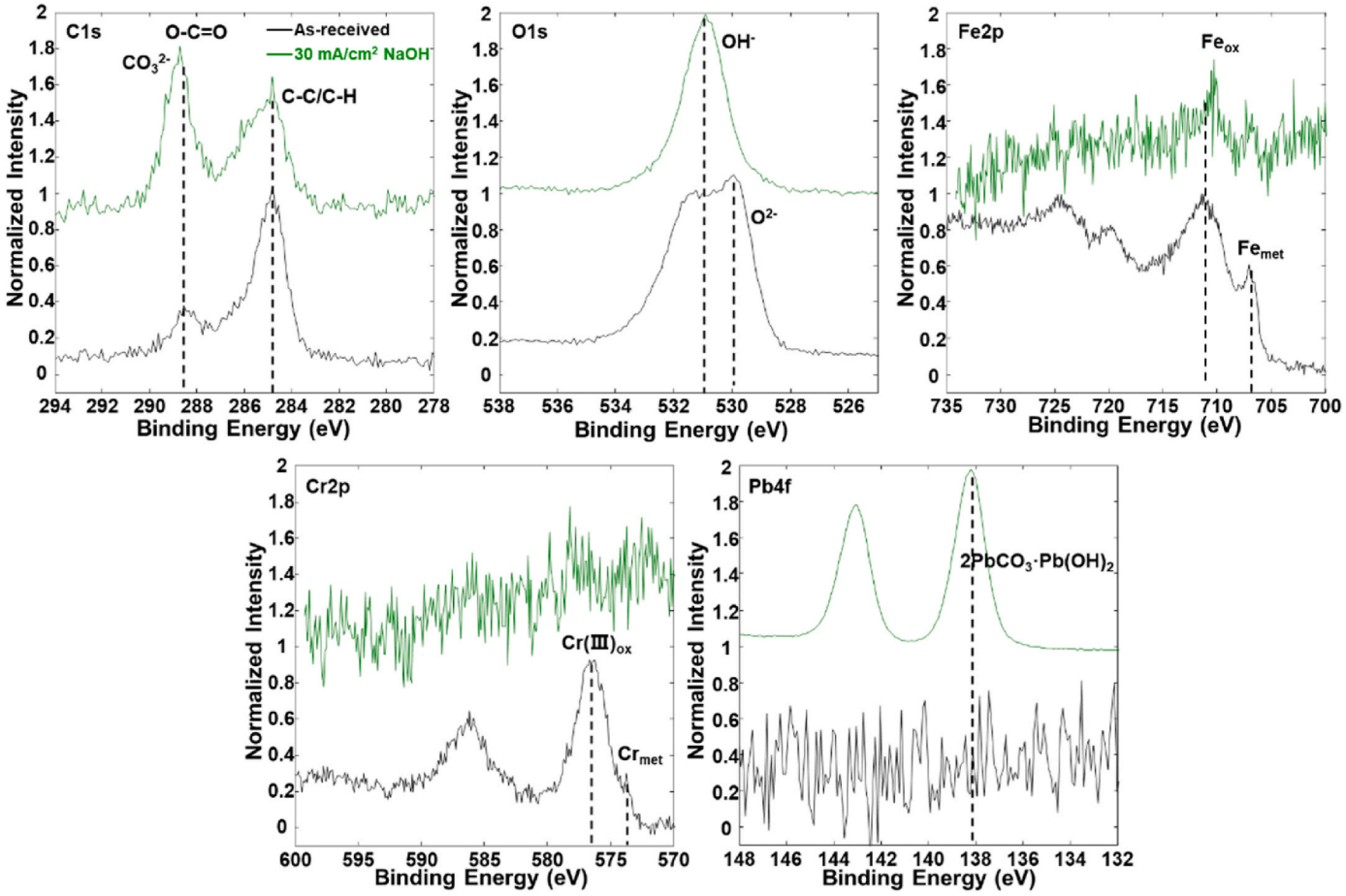

Fig. 11. XPS region spectra of 316L after hydrogen charging in 0.2 M NaOH.

Table 4
Total hydrogen content of samples after cathodic charging in different electrolyte. All samples were polished using a 1 μm diamond suspension before charging.

Electrolyte	0.2 M H_2SO_4	3 wt% NaCl	0.2 M NaOH	0.2 M NaOH[1]
Total H content	17.50 ppm	1.65 ppm	3.33 ppm	2.01 ppm

1: After polishing to remove deposits.

cathodic hydrogen charging is shown in Fig. 12. Protons (H^+) in the electrolyte combine with electrons at the metal surface to form adsorbed hydrogen atoms (H_{ads}), which may be adsorbed physically (weakly) or chemically (strongly). The adsorbed hydrogen can (i) remain adsorbed on the surface; (ii) enter the metal as absorbed hydrogen atom (H_{abs}); (iii) recombine to form molecular hydrogen (H_2). Enhanced recombination (Fig. 12a) due to surface roughening leads to lowered hydrogen absorption and thus lower hydrogen content. In other words, polishing reduces comparatively the recombination rate (Fig. 12b), enabling more hydrogen to enter the steel. On the other hand, grinding with coarse grit introduces substantial surface deformation and residual stress. The resulting high-density dislocations and residual compressive stresses act as hydrogen traps in the surface region, thereby reducing hydrogen permeation (Fig. 12a). In contrast, smooth (polished) surfaces exhibit a lower dislocation density and therefore fewer hydrogen traps, promoting easier hydrogen permeation and uptake (Fig. 12b). Kim et al. [14] used time-of-flight secondary ion mass spectrometry to show that the normalized H^- signal in the subsurface region of rough samples was higher than in smooth sample, indicating a higher density of trapping sites. Complementary thermal desorption spectroscopy demonstrated that the overall hydrogen content of rough samples was lower, confirming that surface roughening suppresses hydrogen uptake. Laureys et al. [31] demonstrated through hydrogen permeation experiments that, in ultra-low carbon steel, the hydrogen diffusivity of recrystallized samples is an order of magnitude higher than that of cold-deformed samples. This is attributed to the high density of dislocations and defects introduced by cold deformation, which act as hydrogen traps and

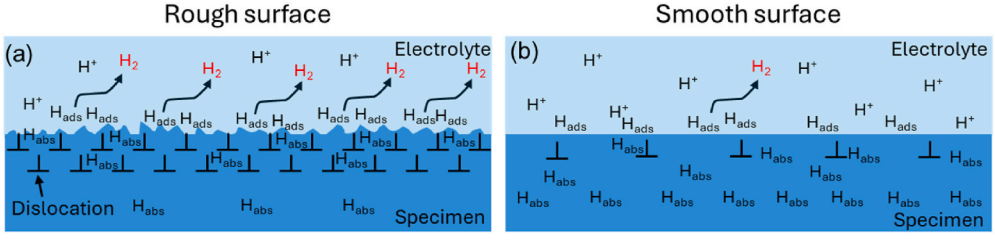

Fig. 12. Schematic H behavior on (a) rough and (b) smooth surfaces.

reduce hydrogen permeation.

As shown in Fig. 3, after hydrogen charging, the rough surface is intact while the smooth surface exhibits severe cracks. Hydrogen charging-induced cracking is influenced by both surface stress and hydrogen content. Hydrogen charging in acidic electrolytes usually has a high hydrogen fugacity, up to 10^8 atm [32]. Rozenak [9] calculated that the maximum tensile stress generated when hydrogen egress from the polished surface of the sample charged in 1 N H_2SO_4 solution was as high as 110 GPa, far exceeding the tensile strength of solution annealed 316L (~610 MPa). Such extreme stresses, combined with high hydrogen concentrations in polished samples, promote surface cracking. In contrast, the residual compressive stress and dislocation density in the mechanically roughened samples inhibit hydrogen absorption and thereby suppress cracking. Li et al. [33] similarly reported that ground surfaces possess a higher residual compressive stress than polished ones, reducing hydrogen-induced blistering in iron. In summary, surface roughening can effectively inhibit hydrogen-induced cracking and reduce hydrogen absorption under electrochemical charging conditions. However, the effectiveness of surface roughening in reducing hydrogen absorption in gaseous hydrogen environments requires further investigation.

4.2. Effects of current density and electrolyte on hydrogen content

Table 3 shows that the hydrogen content increases significantly with increasing current density. Table 4 presents that hydrogen charging in H_2SO_4 solution has the highest hydrogen content followed by NaOH, and NaCl has the lowest. In fact, the surface hydrogen concentration during cathodic hydrogen charging depends on the hydrogen fugacity, following Sievert's law in eq. (7) [34]:

$$C_H = k_s\sqrt{f_{H_2}} \tag{7}$$

Where C_H is hydrogen concentration in the metal, f_{H_2} is hydrogen fugacity or gas partial pressure, k_s is Sieverts' constant (temperature-dependent solubility coefficient). Equation (7) indicates that the hydrogen concentration increases parabolically with the hydrogen fugacity. The effective hydrogen fugacity on the hydrogen-charged surface can be thermodynamically described using the Nernst equation in eq. (8) [35].

$$f_{H_2} = Aexp\left(-\frac{\eta F}{BRT}\right) \tag{8}$$

Where, A and B are empirical constants fitted from experiment. F is the Faraday constant (96485.3 C/mol), R is the gas constant (8.31446 J/(K•mol)), T is the absolute temperature in K, η refers to the overpotential, which can be obtained from eq. (9):

$$\eta = E_C - E_H^0 \tag{9}$$

Where E_C is applied cathode potential, E_H^0 is the equilibrium potential for the hydrogen evolution reaction (HER) at 1 atm, which can be determined from eq. (10) [35]:

$$E_H^0 = -0.0591 \times pH - 000295\ log\ f_{H_2} \tag{10}$$

As shown in Eqs. (8)–(10), hydrogen fugacity is exponentially increased by cathodic overpotential, enhanced at low temperature, and strongly promoted by low pH. In this study, the temperature was kept constant, and the main influencing factors were overpotential and pH value. As can be seen from Eq. (9), the more negative the applied cathode potential, the larger absolute value of the overpotential. Although this study uses constant current control for hydrogen charging, it can be seen from Fig. 4a, 5a and 8a that the higher the current density, the more negative the equivalent applied cathode potential. This means that hydrogen charging at high current density leads to an exponential increase in hydrogen fugacity. According to Eqs. (10) and (9), the smaller the pH value, the more negative E_H^0 becomes, which in turn gives rise to an increase in the absolute value of the overpotential. In summary, increasing the current density and decreasing the pH value leads to a more negative overpotential, thus significantly increasing the hydrogen fugacity. Ref. [32] reported that the hydrogen fugacity of 99.99% iron in 1 N H_2SO_4 at 24 °C with a current density of 4.5 mA/cm^2 is 1.2×10^8 atm. Ref. [36] reported a hydrogen fugacity of 2.2×10^1 atm for Armco iron in 0.1 N NaOH at 25 °C with a current density of 8.1 mA/cm^2. Lu et al. [37] found that for nickel-625 alloys in 0.1 M NaOH at 60 °C, the hydrogen fugacity increased from 5×10^4 atm to 3×10^5 atm as the current density increased from 1 to 30 mA/cm^2. These results demonstrate that hydrogen charging under acidic conditions and at higher current density can significantly enhance hydrogen fugacity.

In this study, hydrogen charging in 0.2 M H_2SO_4 solution at higher current density results in increased hydrogen fugacity, leading to higher hydrogen content, and accompanied surface cracking which intensifies hydrogen diffusion and absorption. In contrast, hydrogen charging in 3 wt% NaCl and 0.2 M NaOH solutions leads to lower hydrogen content without significant surface damage due to lower hydrogen fugacity. Notably, the hydrogen content in the 3 wt% NaCl was only about half that in the 0.2 M NaOH solution, indicating that hydrogen uptake is not a monotonic function of pH. The availability of the hydrogen source is another influencing factor. In the 3 wt% NaCl, hydrogen only comes from the dissociation of H_2O, while in the 0.2 M NaOH solution, both H_2O and OH^- can provide hydrogen. Since H_2O is relatively difficult to dissociate into H^+ and OH^-, hydrogen generation is less efficient in NaCl solution.

4.3. Insights into cathodic hydrogen charging

Cathodic hydrogen charging is one of the most widely used techniques for introducing hydrogen into metals for HE investigations [1–4, 13–15]. In this study, variations in electrolyte type, applied current densities and surface roughness produced distinct surface morphology and chemistry, as well as varying amount of hydrogen uptake, with hydrogen preferentially concentrated in the near-surface region. It is well established that surfaces play a critical role in many key properties of solids, including diffusion, mechanical failure, and the underlying deformation and fracture mechanisms. Consequently, surface modifications induced during hydrogen charging can significantly influence the observed HE response.

Aqueous solutions of H_2SO_4, NaCl and NaOH are the most widely used electrolytes for cathodic hydrogen charging. Although electrolyte concentrations vary across studies, they share one common observation. Hydrogen charging in acidic solutions leads to markedly more severe HE. Zhang et al. [1] systematically evaluated the HE behavior of X65 pipeline steel after hydrogen charging in acidic, neutral, and alkaline electrolytes, simulating various industrial environments. The results showed that the HE susceptibility of X65 steel strongly depended on the charging electrolyte, with acidic electrolytes leading to surface blistering, and highest HE susceptibility, whereas alkaline electrolytes resulted in the lowest HE susceptibility. Similar electrolyte-dependent surface damage has been reported in other alloy systems. Lu et al. [2] showed that cathodic hydrogen charging of Alloy 718 in acidic solution induced slip lines as well as surface and subsurface cracking, which reduced the ultimate tensile strength and promoted brittle fracture. Kuromoto et al. [38] also reported that cathodic hydrogen charging of austenitic stainless steel 304L in 1 N H_2SO_4 solution caused surface cracking and a consequent reduction in fatigue life. These findings underscore that, in addition to hydrogen uptake, surface cracking induced by hydrogen charging in acidic solution plays an important role to embrittle the metals. Surface cracking not only facilitates hydrogen ingress by shortening diffusion paths and increasing the effective surface area, but also act as stress concentrators that can trigger premature failure. As a result, the synergistic effects of charging-induced surface

damage and hydrogen uptake complicate the interpretation of HE test data. Therefore, for reliable evaluation of HE resistance, it is essential to select hydrogen charging conditions that minimize surface cracking. The surface state of H-charged specimens should be carefully inspected prior to mechanical testing.

In contrast, no surface cracking was observed in this study for samples charged in NaCl and NaOH solutions. Surface deposition was detected, especially in NaOH electrolyte. These deposits do not originate from the base metal itself, but rather from trace impurities present in the chemical reagents. Barchiche et al. [39] similarly reported that under cathodic protection of a carbon steel in seawater, magnesium and calcium impurities lead to the formation of aragonite ($CaCO_3$) and brucite ($Mg(OH)_2$) on the cathode surface. This phenomenon was attributed to the local increase in OH^- concentration during hydrogen evolution (refer eqs. (2) and (5)), which promotes the precipitation of $Mg(OH)_2$ via its reaction with Mg^{2+}. Such scale deposits ($CaCO_3$ and $Mg(OH)_2$) form a physical barrier on the metal surface, hindering oxygen diffusion, thereby reducing the current density or sacrificial anode consumption required to maintain effective protection. There are few reports on the deposition of $2PbCO_3{\cdot}Pb(OH)_2$ during cathodic hydrogen charging in NaOH. According to the Pourbaix (E-pH) diagram [40] for Pb–H_2O–CO_3 system, $2PbCO_3{\cdot}Pb(OH)_2$ will form when the pH $\geq$ 8 and the E $\leq$ 1 V. In fact, numerous literature reports that lead in drinking water primarily originate from the corrosion and dissolution of lead-containing pipes [41,42]. Studies have shown that hydrated cerussite ($2PbCO_3{\cdot}Pb(OH)_2$) and cerussite ($PbCO_3$) are widely present in their corrosion scale [43,44]. It should be borne in mind that it is the surface that interacts directly with the environment. Surface deposits can affect hydrogen absorption and HE behavior [45,46]. For instance, deposited Ni and Cd layers have been reported to impede hydrogen diffusion and reduce hydrogen uptake [46]. How the surface deposits originating from trace impurities in chemical reagents influence hydrogen absorption and HE, once formed, has received limited attention in literature. This artifact effect is often overlooked and warrants further investigation in future studies.

Overall, while cathodic hydrogen charging is an effective method for introducing hydrogen into metals, it can introduce undesirable side effects, including surface damage (e.g., cracking) and impurity deposition, depending on the charging conditions and initial surface states. These surface alterations can influence HE behavior and must therefore be carefully considered. Different charging conditions yield distinct hydrogen fugacity, as reflected by variations in hydrogen uptake, with acidic solutions generally promoting more aggressive charging. Reducing the applied current density can mitigate surface cracking and reduce hydrogen absorption. Therefore, excessively high current density should therefore be avoided. Careful control of experimental parameters including electrolyte and current density selection is crucial when using this technique. Surface conditions before and after charging should be examined thoroughly. Ultimately, it is essential to assess whether the adverse effects associated with specific charging conditions can be safely neglected for HE investigation.

5. Conclusions

In this work, 316L ASS was hydrogen-charged cathodically in three electrolytes: H_2SO_4, NaCl and NaOH. The resulting change in surface morphology depended on the charging conditions and the initial surface roughness. In H_2SO_4 solution, the hydrogen content was the highest among the three electrolytes under identical charging parameters, and surface cracking became more severe with increasing current density. Surface roughening significantly reduced hydrogen-induced cracking and hydrogen uptake by promoting hydrogen recombination. When charging in NaOH solution, surface deposits, likely in the form of $2PbCO_3{\cdot}Pb(OH)_2$, were observed. In NaCl solution, a very small amount of $Mg(OH)_2$ is deposited, and the surface morphology was the least affected by current density among the three electrolytes. The deposits formed in neutral and alkaline solution originated from the trace impurities in the electrolyte. These surface changes, including surface cracking and deposition, may influence HE behavior and therefore require careful consideration.

CRediT authorship contribution statement

Xiao Qin: Writing – review & editing, Writing – original draft, Visualization, Methodology, Investigation, Formal analysis, Data curation, Conceptualization. **Yao Shi:** Writing – review & editing, Writing – original draft, Validation, Methodology, Investigation, Formal analysis, Data curation, Conceptualization. **Sri Bala Aditya Malladi:** Writing – original draft, Validation, Investigation, Data curation. **Huiqun Liu:** Writing – original draft, Visualization, Validation, Formal analysis, Data curation, Conceptualization. **Lars Nyborg:** Writing – review & editing, Writing – original draft, Visualization, Validation, Methodology, Investigation, Formal analysis, Data curation. **Yu Cao:** Writing – review & editing, Writing – original draft, Visualization, Validation, Supervision, Resources, Project administration, Methodology, Investigation, Funding acquisition, Formal analysis, Data curation, Conceptualization.

Declaration of competing interest

The authors declare that they have no known competing financial interests or personal relationships that could have appeared to influence the work reported in this paper.

Acknowledgments

This work was financed by the competence center TechForH2 hosted by Chalmers University of Technology and financially supported by the Swedish Energy Agency (P2021-90268) and the member companies Volvo, Scania, Siemens Energy, GKN Aerospace, PowerCell, Oxeon, RISE, Stena Rederier AB, Johnson Matthey and Insplorion, Sweden's innovation agency (2021-01908), Production Area of Advance, Chalmers University of Technology.

References

[1] Zhang P, Laleh M, Hughes AE, Marceau RK, Hilditch T, Tan MY. A systematic study on the influence of electrochemical charging conditions on the hydrogen embrittlement behaviour of a pipeline steel. Int J Hydrogen Energy 2023;48:16501–16. https://doi.org/10.1016/j.ijhydene.2023.01.149.
[2] Lu X, Wang D, Wan D, Zhang ZB, Kheradmand N, Barnoush A. Effect of electrochemical charging on the hydrogen embrittlement susceptibility of alloy 718. Acta Mater 2019;179:36–48. https://doi.org/10.1016/j.actamat.2019.08.020.
[3] Kyriakopoulou HP, Karmiris-Obratański P, Tazedakis AS, Daniolos NM, Dourdounis EC, Manolakos DE, Pantelis D. Investigation of hydrogen embrittlement susceptibility and fracture toughness drop after in situ hydrogen cathodic charging for an X65 pipeline steel. Micromachines 2020;11:430. https://doi.org/10.3390/mi11040430.
[4] Dwivedi SK, Vishwakarma M. Hydrogen embrittlement in different materials: a review. Int J Hydrogen Energy 2018;43:21603–16. https://doi.org/10.1016/j.ijhydene.2018.09.201.
[5] Ďurovič M, Hnát J, Bouzek K. Electrocatalysts for the hydrogen evolution reaction in alkaline and neutral media. A comparative review. J Power Sources 2021;493:229708. https://doi.org/10.1016/j.jpowsour.2021.229708.
[6] Bockris JM, Potter EC. The mechanism of the cathodic hydrogen evolution reaction. J Electrochem Soc 1952;99:169. https://doi.org/10.1149/1.2779692.
[7] Li W, Cao R, Xu L, Qiao L. The role of hydrogen in the corrosion and cracking of steels-a review. Corros Commun 2021;4:23–32. https://doi.org/10.1016/j.corcom.2021.10.005.
[8] Thomas S, Sundararajan G, White PD, Birbilis N. The effect of absorbed hydrogen on the corrosion of steels: review, discussion, and implications. Corrosion 2017;73:426–36. https://doi.org/10.5006/2242.
[9] Rozenak P, Loew A. Stress distributions due to hydrogen concentrations in electrochemically charged and aged austenitic stainless steel. Corros Sci 2008;50:3021–30. https://doi.org/10.1016/j.corsci.2008.08.045.
[10] Li X, Huang W, Wu X, Zhang J, Wang Y, Akiyama E, Hou D. Effect of hydrogen charging time on hydrogen blister and hydrogen-induced cracking of pure iron. Corros Sci 2021;181:109200. https://doi.org/10.1016/j.corsci.2020.109200.

[11] Yu H, Díaz A, Lu X, Sun B, Ding Y, Koyama M, Zhang Z. Hydrogen embrittlement as a conspicuous material challenge–comprehensive review and future directions. Chem Rev 2024;124:6271–92. https://doi.org/10.1021/acs.chemrev.3c00624.
[12] Li X, Ma X, Zhang J, Akiyama E, Wang Y, Song X. Review of hydrogen embrittlement in metals: hydrogen diffusion, hydrogen characterization, hydrogen embrittlement mechanism and prevention. Acta Metall Sin 2020;33:759–73. https://doi.org/10.1007/s40195-020-01039-7.
[13] Queiroga LR, Marcolino GF, Santos M, Rodrigues G, dos Santos CE, Brito P. Influence of machining parameters on surface roughness and susceptibility to hydrogen embrittlement of austenitic stainless steels. Int J Hydrogen Energy 2019; 44:29027–33. https://doi.org/10.1016/j.ijhydene.2019.09.139.
[14] Kim J, Hall D, Yan H, Shi Y, Joseph S, Fearn S, Tasan CC. Roughening improves hydrogen embrittlement resistance of Ti-6Al-4V. Acta Mater 2021;220:117304. https://doi.org/10.1016/j.actamat.2021.117304.
[15] Álvarez G, Arniella V, Belzunce FJ, Rodríguez C. Study of the influence of current density and displacement rate on hydrogen embrittlement using small punch tests. Theor Appl Fract Mech 2023;125:103838. https://doi.org/10.1016/j.tafmec.2023.103838.
[16] Gravier J, Vignal V, Bissey-Breton S. Influence of residual stress, surface roughness and crystallographic texture induced by machining on the corrosion behaviour of copper in salt-fog atmosphere. Corros Sci 2012;61:162–70. https://doi.org/10.1016/j.corsci.2012.04.032.
[17] Cui Z, Liu Z, Wang L, Li X, Du C, Wang X. Effect of plastic deformation on the electrochemical and stress corrosion cracking behavior of X70 steel in near-neutral pH environment. Mater Sci Eng, A 2016;677:259–73. https://doi.org/10.1016/j.msea.2016.09.033.
[18] Krawiec H, Vignal V, Schwarzenboeck E, Banas J. Role of plastic deformation and microstructure in the micro-electrochemical behaviour of Ti–6Al–4V in sodium chloride solution. Electrochim Acta 2013;104:400–6. https://doi.org/10.1016/j.electacta.2012.12.029.
[19] Li W, Li DY. Influence of surface morphology on corrosion and electronic behavior. Acta Mater 2006;54:445–52. https://doi.org/10.1016/j.actamat.2005.09.017.
[20] Brown AP, Krumpelt M, Loutfy RO, Yao NP. The effect of surface roughness on the hydrogen evolution reaction kinetics with mild steel and nickel cathodes. Electrochim Acta 1982;27:557–60. https://doi.org/10.1016/0013-4686(82)85039-1.
[21] Gebremariam GK, Jovanović AZ, Pašti IA. The effect of electrolytes on the kinetics of the hydrogen evolution reaction. Hydrogen 2023;4:776–806. https://doi.org/10.3390/hydrogen4040049.
[22] Fukunaga A. Hydrogen embrittlement behaviors during SSRT tests in gaseous hydrogen for cold-worked type 316 austenitic stainless steel and iron-based superalloy A286 used in hydrogen refueling station. Eng Fail Anal 2024;160: 108158. https://doi.org/10.1016/j.engfailanal.2024.108158.
[23] Hirata K, Iikubo S, Koyama M, Tsuzaki K, Ohtani H. First-principles study on hydrogen diffusivity in BCC, FCC, and HCP iron. Metall Mater Trans A 2018;49: 5015–22. https://doi.org/10.1007/s11661-018-4815-9.
[24] Martin M, Weber S, Theisen W, Michler T, Naumann J. Development of a stable high-aluminum austenitic stainless steel for hydrogen applications. Int J Hydrogen Energy 2013;38:5989–6001. https://doi.org/10.1016/j.ijhydene.2013.02.127.
[25] Rajasekar S, Chetty R, Neelakantan L. Low-nickel austenitic stainless steel as an alternative to 316L bipolar plate for proton exchange membrane fuel cells. Int J Hydrogen Energy 2015;40:12413–23. https://doi.org/10.1016/j.ijhydene.2015.05.194.
[26] Peng Z, Liu J, Huang F, Zhang S, Hu Q, Wang Z, Wang Y. The significance of inclusion morphology and composition in governing hydrogen transportation and trapping in steels. Int J Hydrogen Energy 2021;46:28811–22. https://doi.org/10.1016/j.ijhydene.2021.06.096.
[27] Szklarska-śmialowska Z, Lunarska E. The effect of sulfide inclusions on the susceptibility of steels to pitting, stress corrosion cracking and hydrogen embrittlement. Mater Corros 1981;32:478–85. https://doi.org/10.1002/maco.19810321103.
[28] Skaanvik SA, Henderson JD, Noël JJ, Biesinger MC. Speciation of magnesium surfaces by X-ray photoelectron spectroscopy (XPS). Surf Interface Anal 2025;57: 717–28. https://doi.org/10.1002/sia.70003.
[29] Tian H, Xin J, Li Y, Wang X, Cui Z. Combined effect of cathodic potential and sulfur species on calcareous deposition, hydrogen permeation, and hydrogen embrittlement of a low carbon bainite steel in artificial seawater. Corros Sci 2019; 158:108089. https://doi.org/10.1016/j.corsci.2019.07.013.
[30] Maldonado PSDV, Hernández-Montoya V, Concheso A, Miguel A, Montes-Morán MA. Formation of cerussite and hydrocerussite during adsorption of lead from aqueous solution on oxidized carbons by cold oxygen plasma. Appl Surf Sci 2016;386:381–8. https://doi.org/10.1016/j.apsusc.2016.06.025.
[31] Laureys A, Van den Eeckhout E, Petrov R, Verbeken K. Effect of deformation and charging conditions on crack and blister formation during electrochemical hydrogen charging. Acta Mater 2017;127:192–202. https://doi.org/10.1016/j.actamat.2017.01.013.
[32] Kumnick AJ, Johnson HH. Steady state hydrogen transport through zone refined irons. Metall Trans A 1975;6:1087–91. https://doi.org/10.1007/BF02661363.
[33] Li X, Wang Y, Huang W, Zhang J, Wu X. Effect of surface roughness on hydrogen-induced blister behavior in pure iron. Metals 2020;10:745. https://doi.org/10.3390/met10060745.
[34] Venezuela J, Gray E, Liu Q, Zhou Q, Tapia-Bastidas C, Zhang M, Atrens A. Equivalent hydrogen fugacity during electrochemical charging of some martensitic advanced high-strength steels. Corros Sci 2017;127:45–58. https://doi.org/10.1016/j.corsci.2017.08.011.
[35] Liu Q, Atrens AD, Shi Z, Verbeken K, Atrens A. Determination of the hydrogen fugacity during electrolytic charging of steel. Corros Sci 2014;87:239–58. https://doi.org/10.1016/j.corsci.2014.06.033.
[36] Oriani RA, Josephic PH. Hydrogen-enhanced load relaxation in a deformed medium-carbon steel. Acta Metall 1979;27:997–1005. https://doi.org/10.1016/0001-6160(79)90187-1.
[37] Lu X, Wang D, Johnsen R. Hydrogen diffusion and trapping in nickel-based alloy 625: an electrochemical permeation study. Electrochim Acta 2022;421:140477. https://doi.org/10.1016/j.electacta.2022.140477.
[38] Kuromoto NK, Guimaraes AS, Lepienski CM. Superficial and internal hydrogenation effects on the fatigue life of austenitic steels. Mater Sci Eng, A 2004; 381:216–22. https://doi.org/10.1016/j.msea.2004.04.033.
[39] Barchiche C, Deslouis C, Festy D, Gil O, Refait P, Touzain S, Tribollet B. Characterization of calcareous deposits in artificial seawater by impedance techniques: 3—deposit of $CaCO_3$ in the presence of Mg (II). Electrochim Acta 2003; 48:1645–54. https://doi.org/10.1016/S0013-4686(03)00075-6.
[40] Pan W, Pan C, Bae Y, Giammar D. Role of manganese in accelerating the oxidation of Pb (II) carbonate solids to Pb (IV) oxide at drinking water conditions. Environ Sci Technol 2019;53:6699–707. https://doi.org/10.1021/acs.est.8b07356.
[41] Mohammadzadeh M, Basu OD, Herrera JE. Impact of water chemistry on lead carbonate dissolution in drinking water distribution systems. J Water Resour Protect 2015;7:389–97. https://doi.org/10.4236/jwarp.2015.75031.
[42] Lasheen MR, Sharaby CM, El-Kholy NG, Elsherif IY, El-Wakeel ST. Factors influencing lead and iron release from some Egyptian drinking water pipes. J Hazard Mater 2008;160:675–80. https://doi.org/10.1016/j.jhazmat.2008.03.040.
[43] Kim EJ, Herrera JE. Characteristics of lead corrosion scales formed during drinking water distribution and their potential influence on the release of lead and other contaminants. Environ Sci Technol 2010;44:6054–61. https://doi.org/10.1021/es101328u.
[44] Noel JD, Wang Y, Giammar DE. Effect of water chemistry on the dissolution rate of the lead corrosion product hydrocerussite. Water Res 2014;54:237–46. https://doi.org/10.1016/j.watres.2014.02.004.
[45] Li Y, Barzagli F, Liu P, Zhang X, Yang Z, Xiao M, Zhang R. Mechanism and evaluation of hydrogen permeation barriers: a critical review. Ind Eng Chem Res 2023;62:15752–73. https://doi.org/10.1021/acs.iecr.3c02259.
[46] Kim H, Popov BN, Chen KS. Comparison of corrosion-resistance and hydrogen permeation properties of Zn–Ni, Zn–Ni–Cd and Cd coatings on low-carbon steel. Corros Sci 2003;45:1505–21. https://doi.org/10.1016/S0010-938X(02)00228-7.